Molecular Catalysis xxx (xxxx) xxx–xxx

Contents lists available at ScienceDirect

Molecular Catalysis

journal homepage: www.elsevier.com/locate/mcat

Tailoring the stability and photo-Fenton activity of Fe-modified nanostructured silicates by tuning the metal speciation from different synthesis conditions

Verónica R. Elías[a], Pablo A. Ochoa Rodriguez[a], Eliana G. Vaschetto[a], Gina A. Pecchi[b], Cristián Huck-Iriart[c], Sandra G. Casuscelli[a], Griselda A. Eimer[a,*]

[a] Centro de Investigación y Tecnología Química (CITeQ) CONICET-UTN, Facultad Regional Córdoba, Universidad Tecnológica Nacional, Córdoba, Argentina
[b] Facultad de Ciencias Químicas, Universidad de Concepción, Casilla160-C, Concepción, Chile
[c] Escuela de Ciencia y Tecnología (ECyT), Universidad Nacional de San Martín (UNSAM), San Martín, Provincia de Buenos Aires, Argentina

ARTICLE INFO

Keywords:
Iron speciation
Solvent
Stability
Photo-Fenton

ABSTRACT

The stability and photo Fenton activity of nanoarchitectured silicates modified with Fe by the wet impregnation method were studied as a function of the used solvent, calcination temperature and iron loading. The physicochemical properties were characterized by SAXS, XRD, N_2 physisorption, SEM, AA, UV–Vis DR, XPS and TPR. All solids showed long-range structural order typical of SBA-15 with high specific surface, P_V and a narrow distribution of P_D. The proper choice of impregnation solvent allowed tuning the iron speciation in order to obtain catalysts highly stable and efficient for their use in the azo dyes photo-Fenton degradation at pH = 3.5. Calcination temperature does not seem influence on such speciation. Isolated iron cations finely dispersed and strongly anchored on the mesoporous channels, whose formation is promoted by the use of ethanol and the low iron loading, are proposed as active sites for the photo-Fenton process. Likewise, low iron loadings also favor the higher accessibility of these sites to the reactant molecules (AO7 and H_2O_2). Thus, the highest dye mineralization degree was obtained by an actual iron loading of 1.31% wt. The heterogeneity of the process was confirmed. The more active solid also showed a high stability and reuse capacity, maintaining its performance.

1. Introduction

Nowadays, there is a great variety of organic compounds discharged into watercourses, product of different industrial activities such as the manufacture of leather, rubber and textile production. Among these substances are the azo dyes, whose structures ha azo groups that can react with other substances in the aqueous medium, leading to the formation of even more toxic compounds. Due to their persistent and refractory nature, these dyes are resistant to conventional treatments [1,2]. In this sense, researches have been conducted in order to develop new remediation technologies. Here, Advanced Oxidation Processes (AOPs) emerge as promising strategies. The main goal for these technologies is to generate radical species with high oxidizing power, capable of attacking the organic pollutants reaching their complete degradation and mineralization [3]. Interesting results have been obtained applying homogeneous photo-Fenton process which involves the redox reaction between the Fe^{2+}/ Fe^{3+} species and the H_2O_2, with the subsequent formation of the highly reactive free radical species [4]. Since, homogeneous Fenton processes have the drawback related to the needed of subsequent stages of treatment for the separation of solubilized iron from the liquid effluent, one of the alternatives on the rise involves the anchoring of iron species on porous solids with high specific area [5,6]. This would imply the presence of numerous and available active sites, and in turn, an easy recovery from the reaction medium when the treatment is finished. Nevertheless, the conventional Fenton processes are effective at low pH values (2.8–3) [7,8], which is a negative condition for the stability of the anchored iron species. Thus, when solids materials are used as catalysts for pollutants degradation in aqueous solutions, the leaching of metal species from the solid phase must be considered and tested. The importance of the solid stability involves two important aspects: 1) the leaching of the metal provokes the loss of the catalytic activity due to the decrease in the number of active sites on the solid surface and 2) the leached metal could also be active in homogeneous phase and therefore, this contribution to the observed activity must be determined.

SBA-15 silicates with a long-range hexagonal array of defined size

* Corresponding author.
E-mail address: geimer@frc.utn.edu.ar (G.A. Eimer).

https://doi.org/10.1016/j.mcat.2018.10.012
Received 27 July 2018; Received in revised form 16 October 2018; Accepted 19 October 2018

mesopores present high specific surface resulting very attractive for the anchoring of active metal species [9]. Several methods for the modification of inert supports with iron species exist, which influence on the developed metal species and their stabilization on the structure. In this sense, the wet impregnation post synthesis method, is an effective way for the modification of SBA-15 silicates with catalytically active metal species and has been widely used to prepare supported catalysts. Although the impregnation method is simple and fast, involves several steps that influence notably on the obtained solids and their catalytic activity. Some researchers found that active species formed on catalysts synthetized by the Fe loading on different supports, varied with the calcination temperature, influencing for example, on the selective reduction of NOx with ammonia [9,10]. It has been found that the calcination temperatures affect on the activity of iron oxide phase doped with Mn [11]. Thus, a calcination temperature of 350 °C results in the major formation of γ-Fe_2O_3 which is more efficient to the NO conversion than the α-Fe_2O_3, which appears for calcination temperatures of 450 °C. In the case of metal species supported on mesoporous structures should also be considered that high calcination temperatures can result in the bulky aggregation of oxide species that could cause the collapse of the pore structure.

On the other hand, the wet impregnation method involves the use of a solvent for the metal precursor dispersion on the support structure. In this sense, it has been reported that the solvent for the impregnation could affect the interaction between the developed metal species and the support [12–14]. Tao et al. [15] reported about the influence of the solvent on the catalytic properties of Ni/SBA-15 for CO methanation reaction. They found that ethanol promotes the dispersion of the active Ni species, affecting notably their catalytic activity.

Although the mentioned works reported on the reactivity of catalysts prepared using different calcination temperatures and solvents, we have not found researches about the effect of these parameters on the physicochemical and catalytic properties of iron modified SBA-15 for photo-Fenton heterogeneous degradation processes.

Thus, the present work reports about the influence of impregnation solvent and calcination process employed to prepare iron modified nanoarchitectured silicates, on the solids structure and the dispersion and anchoring of the iron species developed. Likewise, in order to reveal the use possibility of these solids as photo-Fenton catalysts, their stability against metal species leaching under acid conditions of the reaction medium was tested. After determining the optimum synthesis conditions and reaction medium pH value that ensure this stability, the effect of the Fe loading on the speciation and catalytic activity of the SBA-15 solids was studied in the photo-Fenton degradation process of Acid Orange 7, used as a model pollutant molecule.

2. Experimental

2.1. Synthesis

The bare mesoporous molecular sieve, SBA-15, was synthesized according to the following procedure: Pluronic P123 used as the structure-directing agent, were dissolved in a 2 M HCl solution under stirring at 40 °C. Then, tetraethoxysilane (TEOS), the silicon source, was added dropwise to this solution and kept under stirring at 40 °C for 4 h. Then, the mixture was aged without stirring at 40 °C for 20 h and at 80 °C for 48 h. After this treatment the solid product was recovered, washed and dried at 60 °C. Finally, in order to remove the organic template, the solid was submitted to calcination process heating at 1 °C/min until 500 °C maintaining this temperature for 8 h.

The calcined SBA-15 host was modified with iron by the wet impregnation method using solutions of the metal precursor, Fe$(NO_3)_3{\cdot}9H_2O$, in a concentration corresponding to the different nominal iron loadings. In a typical synthesis, the SBA-15 solid was dispersed in the metal solution at room temperature and then, the solvent was slowly removed by rotary evaporation at 50 °C for 30 min. The resulting powder was dried at 60 °C and then submitted to a calcination process. In this point it is important to clarify that, previous to the analysis of the influence of the iron loading, it was studied the influence of the solvent nature used to prepare the metal precursor solution and the calcination process applied. The nominal iron loading chosen for this study was 10 wt.%. The tested solvents were water or ethanol and the applied calcination process was heating at 3 °C/min until 500 °C, maintaining this temperature for 8 h or heating at 3 °C/min until 350 °C, maintaining this temperature for 3 h. The materials were named: Fe/SBA-15(10)T_x, where T indicates the calcination temperature and "x" indicates the used solvent: water (H_2O) or ethanol (ETOH). Between parentheses figures the nominal metal loading of 10 wt.%.

Then, when the precursor solution solvent and the calcination temperature were chosen, the influence of the metal loading was studied. The tested iron loadings were: 1.0, 2.5, 5.0 and 10.0 wt.%. These samples were named: Fe/SBA-15(i)T_x, where "i" indicates the nominal metal loading.

2.2. Characterization

Small Angle X-ray Scattering (SAXS) experiments were carried out using XEUSS 1.0 equipment from XENOCS with a Kα-copper radiation microsource (λ = 1.54 Å). A Pilatus 100 K detector was used with 521 mm sample detector distance. The acquisition time of each pattern was 30 min. One dimensional curves were obtained by radial integration of the 2D isotropic pattern using Foxtrot software. Samples were placed between two Kapton® windows in a holder suitable for powders. The XRD (x-ray diffraction) patterns (at low and high angle) were recorded in a PANalytical X'Pert Pro diffractometer with Cu Kα radiation (λ = 1.5418 Å) in the range of 0.5–6° and 20–80°. SEM (Scanning Electron Microscopy) images were obtained in a JEOL model JSM 6380LV. Gold coverage was applied to make samples conductive. The acceleration voltage was 20 kV. UV–Vis diffuse reflectance spectra (UV–Vis DRs) were recorded using a Jasco 650 spectrometer with an integrating sphere in the wavelength range of 200–900 nm. For the analysis of the metal content influence, the original spectra obtained were fitted by three Gaussian bands using the conventional least squares method. Curve-fitting calculations were useful in determining each band location and relative area, with confidence levels given by $R^2 \geq 0.99$ and $\chi^2 < 0.001$. The metal content was determined by Atomic Absorption spectroscopy (AA) according to the SMEWW-APHA 3111-B in CEQUIMAP from Universidad Nacional de Córdoba. The N_2 adsorption/desorption isotherms were obtained using a Micromeritics TriStar II 3020 V1.03 (V1.03). Samples were previously dried using a N_2 flux for 3 h at 350 °C. The specific surface was determined by the Brunauer-Emmett-Teller (BET) method in the relative pressure (P/P_0) range of 0.1–0.25. The pore diameter (P_D) was calculated by the Barret-Joyner-Halenda (BJH) method applied in the adsorption branch of the isotherm. XPS (X-ray photoelectron spectroscopy) analyzes were performed on a computer equipped with a Multitechnique Specs Dual X-ray source Mg/Al model XR50 and hemispherical analyzer 150 PHOIBOS Fixed transmission mode analyzer (FAT). Spectra were obtained with a power passage of 30 eV and Al anode operated at 100 and 150 W when conditions in the main chamber were adequate. The pressure during the measurement was less than 2.10^{-8} mbar. The reducibility of catalyst was measured by Temperature Programmed Reduction (TPR) experiments in the Micromeritic ChemiSorb 2720 Instruments. In these experiments, the samples were heated from 298 to 1073 K at a rate of 10 °C min^{-1} in the presence of 5% H_2/N_2 gas mixture (25 mL min^{-1} STP), and the reduction reaction was monitored by the H_2 consumption with a built-in thermal conductivity detector (TCD).

2.3. Stability measurements

The stability of solids as a function of the pH (2.8, 3.5, 5.0) was

tested in order to determine the feasibility of their use as heterogeneous catalysts for degradation of organic pollutants in aqueous solutions by photo-Fenton processes. In this way, the solids were submitted to a process mimicking the catalytic run conditions, but in absence of reactant: catalyst concentration = 1 g L^{-1}, peroxide concentration = 75.8 mg L^{-1}, tested pH = 2.8, 3.5 and 5.0 adjusted using H_2SO_4, contact time under stirring = 5, 90 and 300 min, temperature = 25 °C. The two first pH values were chosen due to they are very close to the pH value for the optimum condition of homogeneous Fenton processes [16,17]. The tested pH of 5.0 is the natural pH of the Acid Orange 7 (AO7) azo dye solution, chosen as probe molecules for the catalysts evaluation. The iron content leached from the solid to the reaction medium was determined by applying the o-phenanthroline colorimetric method (3500-Fe) by spectrophotometry at 510 nm [18]. The method consists of the sensitivity of o-phenathroline to form a complex with the Fe^{2+} ions present in solution. Thus, the absorption of the solution treated with this complex agent, at 510 nm, is proportional to the concentration of solubilized Fe^{2+} ions. For the quantification of the total Fe content (Fe^{+2} and Fe^{3+}), the reaction medium was previously treated with a reducing agent in order to convert leached Fe^{3+} to Fe^{2+} ions.

2.4. Catalytic experiments

The photo-Fenton experiments were performed with a photo-reactor which consists of a borosilicate glass tube of 0.85 L capacity with a sintered glass piece placed at the bottom and four UV_A-vis lamps (Actinic BL 20 W, Philips) placed around the tube. These lamps emit a continuum spectrum in the wavelength range between 350 and 400 nm and two bands at 404 and 438 nm (above 380 nm correspond to the visible region). To avoid the radiation scattering, an aluminum foil was placed around the photo-reactor. For temperature control, a tube was placed in the center of the reactor allowing the circulation of refrigeration water. A circulation pump and a thermostated water bath (25 ± 0.2 °C) were used for this purpose. The suspension volume employed in all of the experiments was 0.5 L with an initial concentration of the AO7 and the catalyst of 20 mg L^{-1} and 1 g L^{-1}, respectively. The suspended catalyst in the aqueous system was oxygenated using an air flow of 1 L min^{-1}, which allowed reach a percentage of oxygen saturation of around 90%. Prior to irradiation, the suspension pH was adjusted to the tested value and stirred in the dark for 45 min in order to reach the adsorption/desorption equilibrium. After the adsorption period, the adequate amount of H_2O_2 was added and an initial sample was extracted to calculate the initial concentration of AO7 and H_2O_2. Then, the reactor was irradiated in order to start the experimental run. Samples were periodically collected and filtered. The [AO7] was monitored by measuring the absorbance at λ of 485 nm using Jasco 7800 spectrophotometer. The [H_2O_2] was determined by applying the modified iodometric titration [19]. The organic pollutant mineralization was measured determining the changes of the Total Organic Carbon (TOC) concentration using a TOC Analyzer Schimadzu 5050.

3. Results and discussion

Fig. 1 shows the X-ray scattering patterns (SAXS) for the bare SBA-15 and those modified with an iron loading of 10 wt.%, employing different solvents and calcination temperatures. SAXS curves indicate the presence of long range positional order. The positions of the peaks in the reciprocal space relative to the position of the first peak are 1: √3: √4, characterizing a two-dimensional hexagonal network in the plane normal to the cylindrical pores. The curves are shown in a semi-log scale in order to clarify the second and third order. The lattice parameter 'a_{hex}' was obtained from the distance between the reflections: $d(hk) = a_{hex}/(h^2 + k^2 + hk)^{1/2}$ by a non-linear least square routine using a summation of Lorentzian functions where the relative peaks position were constrained by the 2D hexagonal network progression [20]. The lattice parameter for bare SBA-15 was 9.94 nm (Table 1). There were a slightly shrink in the hexagonal structure when iron is loaded within the material as it is shown in Table 1. The full width at half maximum (FWHM) of Fe/SBA-15(10.0)500_{H2O} and Fe/SBA-15(10.0)350_{ETOH} from the first diffraction order peak (1,0) decrease in a factor of two from the Fe/SBA-15(10.0)350_{H2O}, in consequence, these samples presented longer range order. Moreover, it was possible to assigned the (2,1) and (3,0) reflections which appear at a relation of √7 and √9 from the first peak, those peaks were negligible in Fe/SBA-15(10.0)350_{H2O}. Nevertheless, all of the solids showed good structural order beyond the solvent used or the applied calcination process.

Fig. 2 shows the high angle XRD patterns of the samples. Here, it could be corroborated the presence of hematite nanoparticles (α-Fe_2O_3) formed on the external surface of the materials synthetized using water as solvent [21,22]. On the other hand, when ethanol is used as solvent, the lack of peaks corresponding to the presence of hematite crystallites indicates that, if this phase is present, it would be of a very small crystallite size or it is an amorphous phase.

Fig. 3 shows N_2 adsorption-desorption isotherms of the samples determined at 77 K and Table 1 reports the corresponding specific surface, pore volume (P_V) and pore diameter (P_D). As it can be observed, all these parameters display values typical of SBA-15 structures. Considering the IUPAC classification, all solids exhibited type IV isotherms which are reversible until relative pressures (P/P_0) around of 0.5/0.6 and show H1 hysteresis loops, typical for mesoporous materials with SBA-15 structure. According to Barrera et al. [23] the adsorption at low relative pressures is due to the filling of micropores or to the strong interaction between adsorbate and adsorbent. At intermediate P/P_0 values, the adsorption is due to mono- or multi-layer adsorption of N_2 on the mesopore walls. Then, the capillary condensation on primary mesopores starts at P/P_0 higher than 0.7 where these mesopores start to fill. For these samples, it is important to note that the observed pronounced inflection at this P/P_0 evidences a well-defined primary mesopore size. Moreover, the close position in the capillary condensation for all solids indicates the similarity in the primary mesopore diameters. The hysteresis loops in the desorption branches show a sharp fall at P/P_0 around 0.7 except for sample impregnated with an aqueous solution and calcined at 500 °C. This last sample exhibits an extended hysteresis loop that is closed at around 0.45. This fact can be due to a partial blocking of the mesopores by the hematite particles already evidenced by XRD. On the other hand, the vertical and parallel adsorption and desorption branches in the hysteresis loops give account for the presence of cylindrical pores with uniform sizes in the SBA-15 support. This feature is only slightly affected by the iron impregnation. Finally, the presence of a plateau in the isotherms at P/P_0 higher than 0.8, could be consequence of the decrease in the external surface arising from the improved alignment of the pores. Then, the higher slope observed for the Fe/SBA-15(10)350_{H2O} would evidence the slightly lower structural order showed by SAXS analysis (Fig. 1). Thus, considering the complete analysis, it can be inferred the following facts: 1) the slight decrease in the specific surface of the Fe/SBA-15(10)350_{H2O} sample with respect to the bare SBA-15, would be due to the lower structural order evidenced by SAXS and by the increased slope of the isotherm at P/P_0 higher than 0.8; 2) the slight decrease in the surface for the Fe/SBA-15(10)500_{H2O} could be attributed to the partial blocking of mesopores (evidenced by the extended hysteresis loop) probably due to the presence of hematite nanoparticles (evidenced by XRD); 3) the slight decrease in the surface and the lower P_D observed for the Fe/SBA-15(10)350_{ETOH} probably result from the presence of finely dispersed iron oxide species on the internal pores surface.

The Scanning Electron Microscopy (SEM) images of the synthetized solids are shown in Fig. 4. For the bare SBA-15, a morphology consistent with elongated (fiberlike) particles could be observed, which is frequently found in this type of structure [24]. This morphology was retained when iron was incorporated using water as solvent. Nevertheless, when ethanol was used as solvent for the iron impregnation,

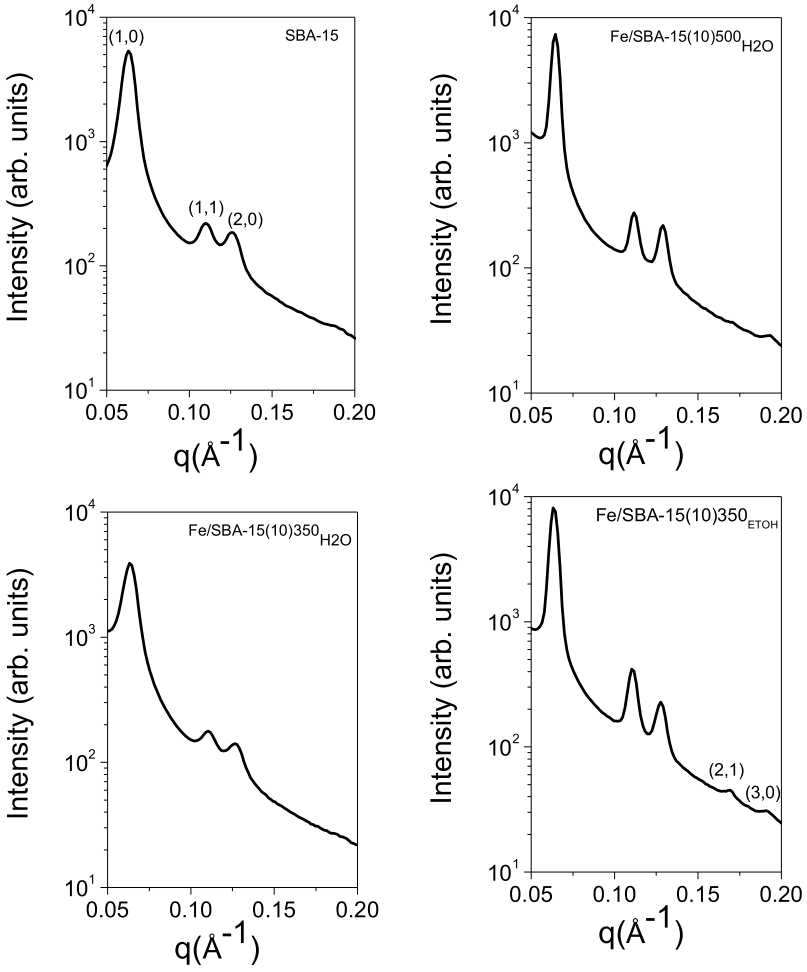

Fig. 1. SAXS patterns of synthetized solids.

Table 1
Hexagonal 2D Lattice parameter 'a_{hex}' and FWHM from the first diffraction order obtained from SAXS patterns and physicochemical properties of the materials synthetized with different solvent and under different calcination process.

Sample	a_{hex} (nm)	FWHM (nm^{-1})	S_{BET} ($m^2 g^{-1}$)	P_V (cm^3/g)	P_D[a] (nm)	Fe[b] (wt.%)
SBA-15	9.94	0.080	839	1.11	7.03	–
Fe/SBA-15(10.0)500_{H2O}	9.87	0.045	716	0.83	7.08	6.57
Fe/SBA-15(10.0)350_{H2O}	9.92	0.092	675	0.85	7.13	6.35
Fe/SBA-15(10.0)350_{ETOH}	9.75	0.047	708	0.81	6.34	6.66

[a] P_D by BJH in the adsorption branch.
[b] Determined by AA.

spongelike morphology was observed. This fact gives evidence of the solvent influence on the particles agglomeration.

The UV–Vis DR spectroscopy was used in order to study the localization and environmental coordination of Fe^{3+} ions present in the SBA-15 structures, as a function of the synthesis conditions (Fig. 5). The spectra are the result of the absorption in three different regions: 200–310, 310–450 and 450–650 nm [25]. The first region with a maximum at around 254 nm corresponds to the dπ-pπ charge transfer between Fe^{3+} and O^{2-} indicating that Fe atoms are linked to O atoms of the silica resulting in the presence of isolated Fe^{3+} on the surface. The second region is usually attributed to the presence of small iron oxides such as nanoclusters (FeO)n. Meanwhile the absorption in the third region that extends to wavelengths longer than 500 nm is assigned to the presence of bigger iron oxide (probably α-Fe_2O_3 nanoparticles). In Fig. 5 it could be observed the increased absorption for the second and the third region when water was used as solvent in the support impregnation. Moreover, comparing with the spectrum of the sample prepared using ethanol (Fe/SBA-15(10)350ETOH), a shifting of the maxima to longer wavelengths could be seen. This fact, taking in mind that a quantum size effect arising from the species sizes decreasing provokes the UV–Vis DR bands shift to shorter wavelengths [26], is another evidence of the presence of metal oxide species of bigger size when water is used as solvent. Moreover, it is notable that the calcination temperature (350 or 500 °C) had not influence on the metal species developed in the silicate structure.

Then, the combined analysis of N_2 physisorption and UV–Vis DR spectroscopy allows suggesting that using ethanol as solvent favors the formation of metal species on the internal walls of the mesopores, which would cause the observed decrease in the P_D. Meanwhile, samples impregnated in presence of water also showed a decrease in the surface and P_V, but P_D value was similar to that of the SBA-15 support. This fact could be associated with certain degree of segregation and

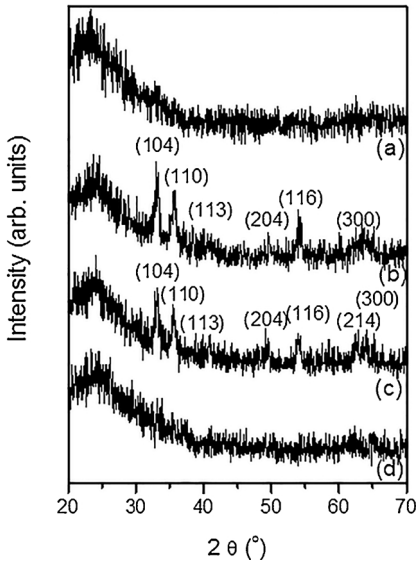

Fig. 2. High angle x-ray patterns of the solids: a) SBA-15, b) Fe/SBA-15(10)500_{H2O}, c) Fe/SBA-15(10)350_{H2O}, d) Fe/SBA-15(10)350_{ETOH}. Between parenthesis were identified the diffraction planes corresponding to the presence of the Fe_2O_3 hematite phase, (330664, Joint Committee on Powder Diffraction Standards).

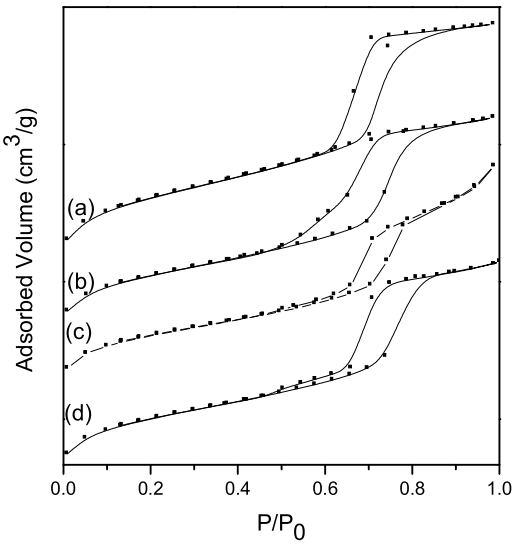

Fig. 3. N_2 adsorption-desorption isotherms of the solids: a) SBA-15, b) Fe/SBA-15(10)500_{H2O}, c) Fe/SBA-15(10)350_{H2O}, d) Fe/SBA-15(10)350_{ETOH}.

agglomeration of Fe species from the inner of the mesopores toward the external surface, resulting in bigger metal species that could be blocking some pore mouths and reducing surface and P_V.

Therefore, a predominant influence of the used solvent on the iron speciation was found, instead of the slight effect produced by the calcination temperature. Thus, although lower calcination temperatures were expected to produce more dispersed species [27], this was not observed here. The Fe-modified samples using water as solvent lead to more segregated iron species of bigger size, for both low and high calcination temperatures. For its part, it has already been reported the influence of the solvent polarity on the metal species dispersion [15]. Molecules of water with high polarity can form a layer onto the silicate surface since they strongly interact with the silanol groups on the SBA-15 surface by H-bonds. Instead, a solvent of less polarity as ethanol forms weaker H-bonds with the silanol groups, allowing that water ligands of hydrated ferric precursor interact directly with the surface by means of H-bonds. In this way the anchoring and the dispersion of iron precursor on the support is promoted by the use of ethanol. This feature could result in a higher stability of the iron species on the solid.

The solids presented in this work were synthesized for their application as catalysts in organic pollutants degradation by the photo-Fenton process. It is important to take into account that the optimal conditions for this process in homogeneous phase include the use of hydrogen peroxide as oxidant at low pH (around 2.8) [16,17]. Therefore, the solids stability to the metal leaching as a function of the pH (2.8, 3.5, 5.0) should be studied in order to determine the feasibility for their used as photo-Fenton heterogeneous catalysts. Thus, the solids were submitted to a treatment mimicking the catalytic run conditions, but in absence of reactant: catalyst concentration = 1 g L^{-1}, H_2O_2 concentration = 75.8 mg L^{-1} and tested pH = 2.8, 3.5 and 5.0, adjusted using H_2SO_4 solution contact time under stirring = 5, 90 and 300 min, temperature = 25 °C. The first tested pH value was chosen due to it is the optimal pH for the homogeneous Fenton process. The second value was chosen in order to test an intermediate pH value and the last value of 5.0 is the natural pH of the Acid Orange 7 (AO7) azo dye solution, chosen as a probe molecule for the catalyst evaluation. From the characterization results presented until now, it was inferred that the calcination temperature does not affect the metal speciation developed on the solids. Therefore, stability was evaluated for those solids prepared using ethanol or water as solvent for the iron-impregnation and calcined at 350 °C. Figs. 6 presents the percentage of iron leached with respect to the initial iron content in Fe/SBA-15(10)350_{H2O} and Fe/SBA-15(10)350_{ETOH} as a function of the pH and stirring time. For all the tested pH values, the higher stability is observed for the sample prepared using ethanol. Here, the higher iron leaching was around 0.9% for the longest stirring time and the lower pH. Meanwhile, the solid prepared using water as solvent was more sensitive to the pH changes. An increase in the acidity provoked a high iron leaching which, for a pH of 2.8, was around 16%. At an intermediate pH of 3.5, iron started to leach from the solid for a stirring time higher than 90 min.

The notable differences in the stability of solids prepared using water or ethanol could be related with the different interaction of the support with metal species as a consequence of their different size, location and dispersion on the structure. Therefore, the higher stability for Fe/SBA-15(10)350_{ETOH} would be associated to the presence of finely dispersed iron oxide species strongly linked to the silica surface. Meanwhile, for Fe/SBA-15(10)350_{H2O} the bigger iron oxides segregated on the external surface result more accessible and sensitive to the leaching.

In order to continue the study about the solid performance as photo-Fenton catalysts, the influence of iron loading on the metal species developed and their impact on the catalytic activity were tested. Here, the employed solids were those synthetized under the optimized impregnation conditions: use of ethanol as solvent and calcination at 350 °C for 3 h.

Figs. 7 shows the XRD patterns at low and high angle for the samples modified with different iron loadings. For all samples the low angle XRD patterns for all samples (Fig. 7A) show peaks corresponding to planes (100), (110) and (200) characteristic of the *p6mm* hexagonal arrangement of SBA-15 silicates, giving evidence of the long range structural order of the solids. The high angle XRD patterns (Figs. 7B) show no peaks, evidencing that the metal species developed on the structure, for all the metal loadings, have a crystallite size below the limit detection of the technique or are in an amorphous phase.

The corresponding N_2 adsorption/desorption isotherms are depicting in Fig. 8 and Table 2 reports the data obtained from this analysis. For all the metal loadings the isotherms are type IV with H1 hysteresis loops characteristic of SBA-15 solids. Pronounced slopes corresponding to the capillary condensation on primary mesopores evidence the narrow pore size distribution. The decrease in the surface and Pv, as well as an increase in the pore wall thickness (W_T) with the

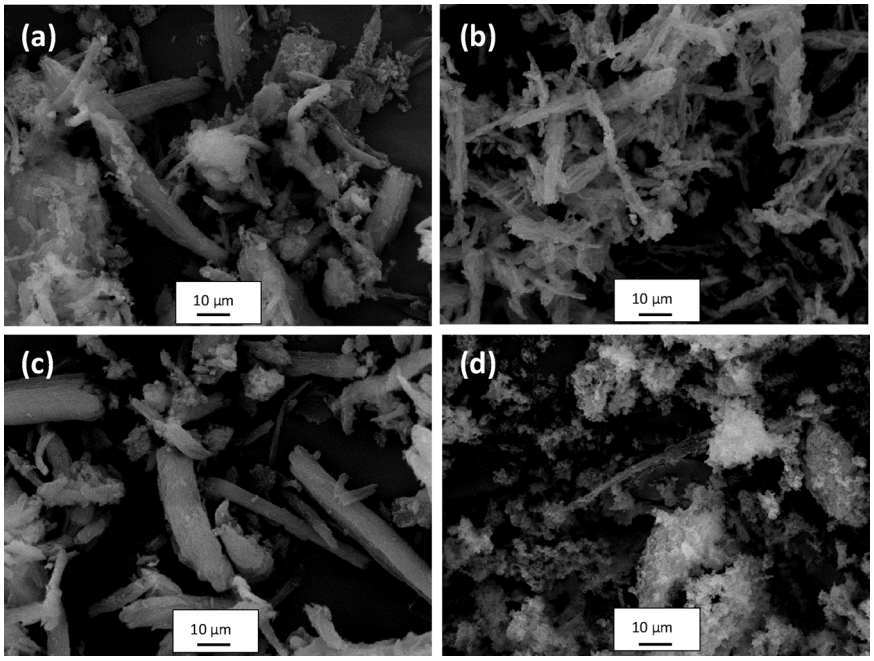

Fig. 4. Scanning electron microscopy (SEM) images of samples: (a) SBA-15, (b) Fe/SBA-15(10)500$_{H2O}$, (c) Fe/SBA-15(10)350$_{H2O}$, (d) Fe/SBA-15(10)350$_{ETOH}$.

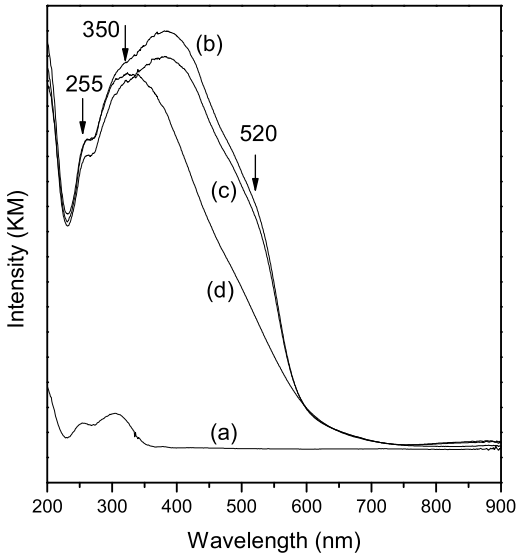

Fig. 5. UV–Vis DR spectra of solids a) SBA-15, b) Fe/SBA-15(10)500$_{H2O}$, c) Fe/SBA-15(10)350$_{H2O}$, d) Fe/SBA-15(10)350$_{ETOH}$.

Fe loading increasing give account for the incorporation of the metal species inside mesoporous channels.

Fig. 9 shows SEM images for samples modified with several iron loadings. A mix of fibers and spongelike morphology could be observed for samples with the lower metal loadings. As the metal loading is increased the spongelike morphology predominates, evidencing the effect of the iron impregnation with ethanol on the particles agglomeration.

By means of UV–Vis DR spectroscopy the influence of the metal loading on the metallic species developed on the silicate structure was analyzed. The original spectra have been fitted with three bands to facilitate the assignments of the different iron species (Fig. 10). The overall metal content in the final solids as well as the relative distribution of the different iron species and an estimation of the iron percentage in these species, are presented in Table 3. The three principal species are the already described: isolated Fe^{3+} cations, smaller iron oxides such as nanoclusters (FeO)n and bigger oxide as nanoparticles (not observed by XRD Fig. 7B). Although the amount of all metal species (Fe wt.%) increases with the iron loading, for the lower ones the proportion of isolated Fe^{3+} ions linked to the surface is higher. Then, even as the presence of nanoclusters is predominant for all the samples, a higher relative percentage of bigger oxide is observed for the iron loading (% area in Table 3). In this sense, the development of the different species as a function of the metal loading could be considered

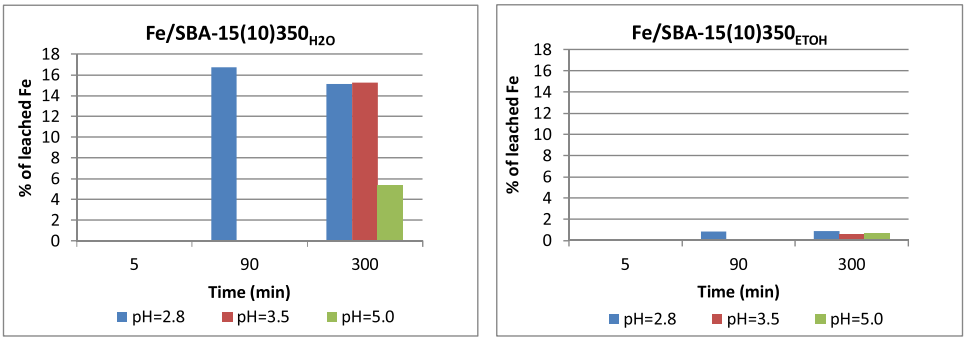

Fig. 6. Percentage of Fe leaching as a function of pH and stirring time for solid synthetized with water or ethanol as solvent.

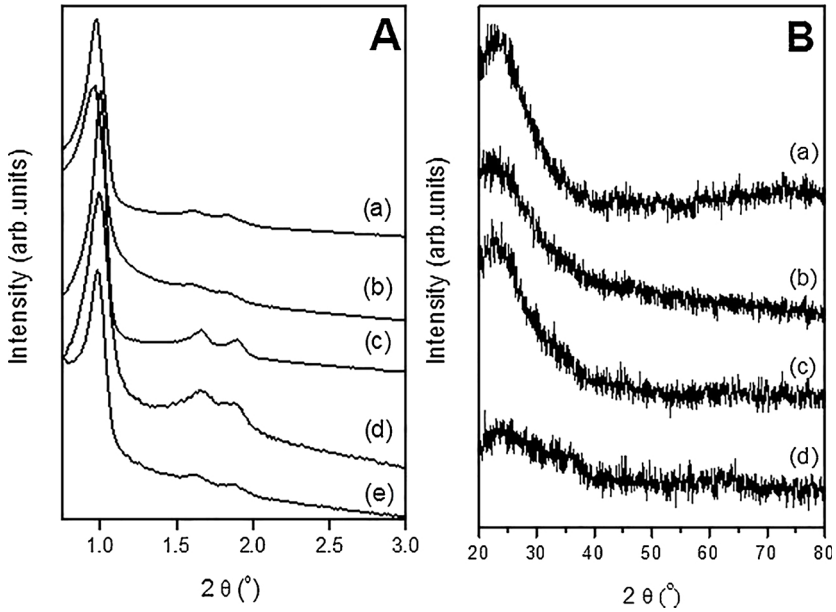

Fig. 7. A) Low-angle XRD patterns and B) high-angle patterns of samples: a) SBA-15, b) Fe/SBA-15(1.0)350$_{ETOH}$, c) Fe/SBA-15(2.5)350$_{ETOH}$, d) Fe/SBA-15(5.0) 350$_{ETOH}$, c) Fe/SBA-15(10.0)350$_{ETOH}$.

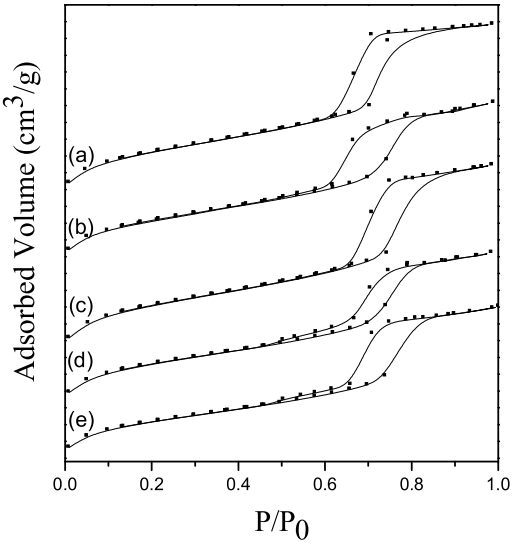

Fig. 8. N_2 adsorption-desorption isotherms of the solids: a) SBA-15, b) Fe/SBA-15(1.0) 350$_{ETOH}$, c) Fe/SBA-15(2.5) 350$_{ETOH}$, d) Fe/SBA-15(5.0) 350$_{ETOH}$, c) Fe/SBA-15(10.0) 350$_{ETOH}$.

Table 2
Physicochemical properties of solids synthetized with different iron loadings.

Samples	Area (cm^2/g)	P_D[a] (nm)	P_V (cm^3/g)	Wall Thickness (Wt)[b] (nm)
SBA-15	893	7.03	1.11	3.39
Fe/SBA-15(1.0)350$_{ETOH}$	887	7.13	1.06	3.31
Fe/SBA-15(2.5)350$_{ETOH}$	863	6.45	1.00	3.77
Fe/SBA-15(5.0)350$_{ETOH}$	778	6.45	0.99	3.80
Fe/SBA-15(10.0)350$_{ETOH}$	708	6.34	0.81	4.04

[a] P_D by BJH in the adsorption branch.
[b] Wt = a_0 − Dp.

as follows. For lower metal contents the isolated Fe^{3+} ions are linked to the surface by the anchoring with the O of the structure. When the iron loading increases, the number of isolated Fe^{3+} ions linked to the surface also increases. These species become closer giving rise to an incipient oligomerization which result in the formation of a major proportion of small nanoclusters (FeO)n. Then, when the iron loading further increases and it exceeds the saturation coverage of the support surface, the nanoclusters grow resulting in the formation of bigger species such as nanoparticles. This fact is notorious for the sample with the highest metal loading where the relative percentage of iron oxide nanoparticles increases at the expense of isolated species (% area in Table 3).

XPS spectra were measured in order to obtain information about the surface composition of the mesoporous support modified with different metal loadings. The XPS spectra were analyzed with the CasaXPS (Casa Software Ltd, UK) software [28]. The spectra were calibrated using the C1s peak correction. The peak areas were determined using Shirley background integration. The peaks were considered as a mixed of Gaussian and Lorenztian functions. The spectra in the Fe 2p region were fitted with several peaks assigned to the Fe^{3+} chemical state (Fig. 11). It is important to note the low intensity of the signal in the Fe region, which could be due to the low metal concentration in the samples. Then, the peaks in Fig. 11 are broader compared with the narrow lines frequently observed for bulk oxides. This fact could be taken as evidence of presence of the highly dispersed metal species on the structure. According to literature, for the Fe_2O_3 standard sample, the binding energy of Fe $2p_{3/2}$ that emerges at around 710 eV, is usually accompanied by a satellite line which is located at around 8 eV higher than the main Fe $2p_{3/2}$ peak. This peak is usually narrower and stronger than the Fe $2p_{1/2}$ peak which is frequently located at 13.5 eV higher [29–31]. Data obtained from the fitting in the iron region are reported in Table 4. Here, it could be observed the presence of the Fe $2p_{3/2}$ peak at around 710 eV, accompanied by a satellite line visible at around 715 eV, and the binding energy of Fe $2p_{1/2}$ peak at around 724 eV which has a satellite line at around 728 eV. All these peaks are indicative of the Fe^{3+} presence in oxide environment [26]. Nevertheless, it is interesting to note that the binding energies difference between the Fe $2p_{3/2}$ peak and its satellite is around 5 eV, notably lower than the expected of 8 eV. The shift of the satellite line could be taken as evidence that the iron species developed on the silicate surface does not correspond to bulk hematite oxide. In fact, it has been reported by Grosvenor et al. [32] that the difference in energy separation between the main peak Fe $2p_{3/2}$ and its satellite decrease when the electronegativity of the ligands decreased. Then, when the metal center is lower coordinated, the electron density

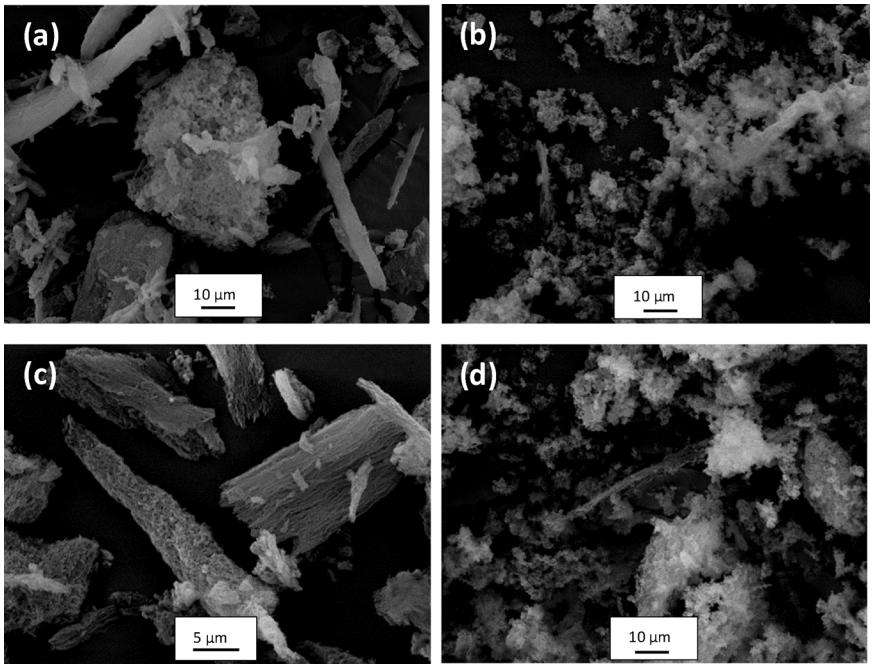

Fig. 9. Scanning electron microscopy (SEM) images of samples: (a) Fe/SBA-15(1.0)350$_{ETOH}$, (b) Fe/SBA-15(2.5)350$_{ETOH}$, (c) Fe/SBA-15(5.0)350$_{ETOH,}$ (d) Fe/SBA-15(10.0)350$_{ETOH}$.

surrounding it increases and lower energy is needed for the 3d electron promotion. In addition, these authors also report the presence of a "surface peak" at the mentioned binding energy (715 eV) which is assigned to the presence of lower coordinated Fe^{3+} ions present in the surface. Therefore, in concordance with the mentioned, the presence of this peak in the XPS spectra of our samples can be related to the presence of isolated Fe^{3+} cations linked to surface O atoms on the matrix or present in small clusters. Both species were already evidenced by UV–Vis DR spectroscopy. In this sense, judging by the lack of an oxygen signal attributed to iron oxides (such as Fe_2O_3) in the spectrum of O 1s (Fig. 12), it could be possible to infer the predominant presence of Fe^{3+} in oxide environment as oligonuclear (FeO)n nanoclusters with lower oxygen coordination. Nevertheless, taking in mind the very low iron content in all solids and the preponderance of oxygen from the silica matrix, the presence of a very small amount of oxide nanoparticles cannot be discarded (as it is evidenced by UV–Vis DR). Finally, all materials showed very similar spectra in the Si 2p region (Fig. 12) which corresponds to the silicates of the mesoporous structure.

On the other hand, Table 4 shows the surface Fe/Si atomic ratios from XPS for all samples obtained from the original spectra fitted. It is known that the Metal/Si ratio could be considered as an indicative of the metal dispersion on the support [33]. Then, an increase in the surface Fe/Si atomic ratios with the increased metal loading could be observed. Nevertheless, for the higher iron loaded samples this surface ratio was markedly lower than the bulk. This feature can be considered as a further evidence of the iron species incorporation inside the mesopores which would be causing the increase in the W_T observed.

It is known that the reduction behavior of metal species deposited on mesoporous supports depends on the interaction of these species with the surface. This interaction is stronger for smaller sized species resulting hardly reducible [34]. In order to analyze the reduction profiles of the synthesized materials it is important to take into account that H_2 consumption associated with the reduction of metal species can be visualized if: 1) the interaction strength of the metal species with the support permits the reduction in the range of temperatures applied, and 2) the metal species are in sufficient quantity to H_2 consumption is detected.

The profiles for all samples show an H_2 consumption at low temperature (around 370 °C) which decreases with the metal loading decreasing (Fig. 13). This first reduction temperature can be assigned to Fe^{3+} ions present in iron oxide species, which weakly interact with the support surface and are partially reduced to $Fe^{3+/2+}$. Although these species are reduced at low temperature, it is interesting to note the shifting of the maximum to higher values for the samples with lower metal loadings, from 370 to 393 °C. This behavior would be evidencing a more difficult reducibility of Fe^{3+} ions, present in these oxide species, stronger linked to the surface O atoms when the metal loading is lower. On the other hand, besides that for the highest iron loaded sample the H_2 consumption is markedly higher, the notorious shoulder arising at 445 °C can be assigned to the further reduction of $Fe^{3+/2+}$ to Fe^{2+}. This gives account for the lower interaction of these oxides with the support, as a consequence of their increased size from the higher iron content [35]. Thus, the TPR profiles for all the materials evidence the increase in the amount, and reducibility of iron oxides when the metal loading increases. However, it is important to note that these oxides have not the reduction behavior of the bulk hematite. This could be due to they are smaller nanoparticles that stronger interact with the support hindering their reducibility. In addition, these species could also be in an amorphous phase, probably as (FeO)n clusters, which are lacking of a defined crystalline structure. Lazar et al. already observed the mentioned species in mesoporous materials with MCM-41 structure [36].

For the two higher iron loaded samples a new H_2 consumption at 605 °C arises. This peak could be associated to the presence of isolated Fe^{3+} ions, whose reducibility depends on the number of Fe-O-Si bonds in their first coordination sphere which influences on the species stabilization. In this sense, the evolution of this isolated species can be considered as follows. When the iron content is low the Fe^{3+} ions could be linked to multiple O atoms of the surface stabilizing and resulting resistant to the reduction. Thus, these ions result not reducible in the evaluated temperature range for Fe/SBA-15(1.0) and Fe/SBA-15(2.5) samples, due to their high stability. It could be inferred that the coordination sphere of the Fe^{3+} ions is saturated and the linked ions on the surface are protected by the silica framework hindering their reduction. For the higher iron loadings, the Fe—O—Si bonds start to be closer giving rise to polymerization reactions and formation of a Fe—O—Fe bond network [37,38], where the metal ions are less bonded

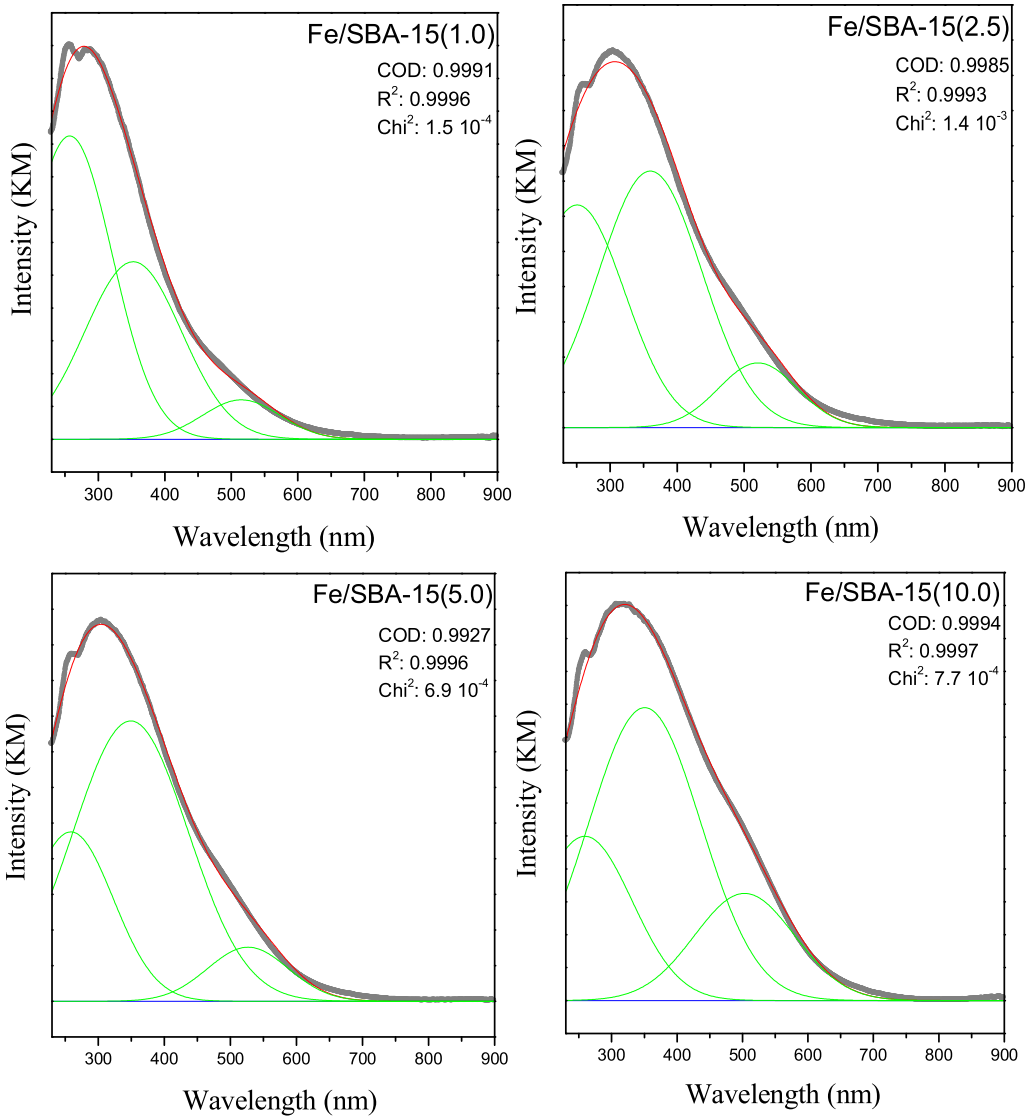

Fig. 10. UV–Vis DR spectra of samples synthetized with different iron loading.

with the support. Therefore, the presence of H_2 consumption at high temperature (605 °C) for samples with the highest iron loadings could be associated to reduction of Fe^{3+} ions with lower coordination degree with the support, less stabilized and of easier reducibility.

It is important to highlight the notably higher H_2 consumption at the complete range of temperatures for the samples presented here with respect to those synthetized from silicates with MCM-41 structures [26,34]. Although the iron species are strongly linked to the surface in both silicate supports, the SBA-15 molecular sieves have pore diameters of almost twice that those of MCM-41. This feature would allow the easier diffusion of the H_2 molecules reducing in a greater proportion the metal species.

Fig. 14 and Table 5 show the results of the catalytic evaluation in the azo dye (AO7) degradation at pH = 3.5 for all iron modified materials using ethanol as the impregnation solvent. It is important to clarify that under this pH the solid modified with the highest iron loading was stable to the metal leaching. For all of the tested catalysts, complete AO7 and H_2O_2 conversion were reached. However, the influence of the metal content on the mineralization degree was evident (Table 5), increasing up to 80% when the nominal content increases

Table 3
Chemical composition and relative distribution of iron species in samples synthetized with different metal loadings.

Sample	Iron content (wt. %)[a]	Distribution of iron species					
		Isolated Fe^{3+}		Smaller iron oxides (nanoclusters)		Bigger iron oxides (nanoparticles)	
		% area	Fe wt. %	% area	Fe wt. %	% area	Fe wt. %
$Fe/SBA\text{-}15(1.0)350_{ETOH}$	0.47	47	0.22	45	0.21	8	0.04
$Fe/SBA\text{-}15(2.5)350_{ETOH}$	1.31	30	0.39	58	0.76	12	0.16
$Fe/SBA\text{-}15(5.0)350_{ETOH}$	3.80	22	0.84	68	2.58	10	0.38
$Fe/SBA\text{-}15(10.0)350_{ETOH}$	6.66	16	1.07	63	4.20	21	1.40

[a] Determined by AA.

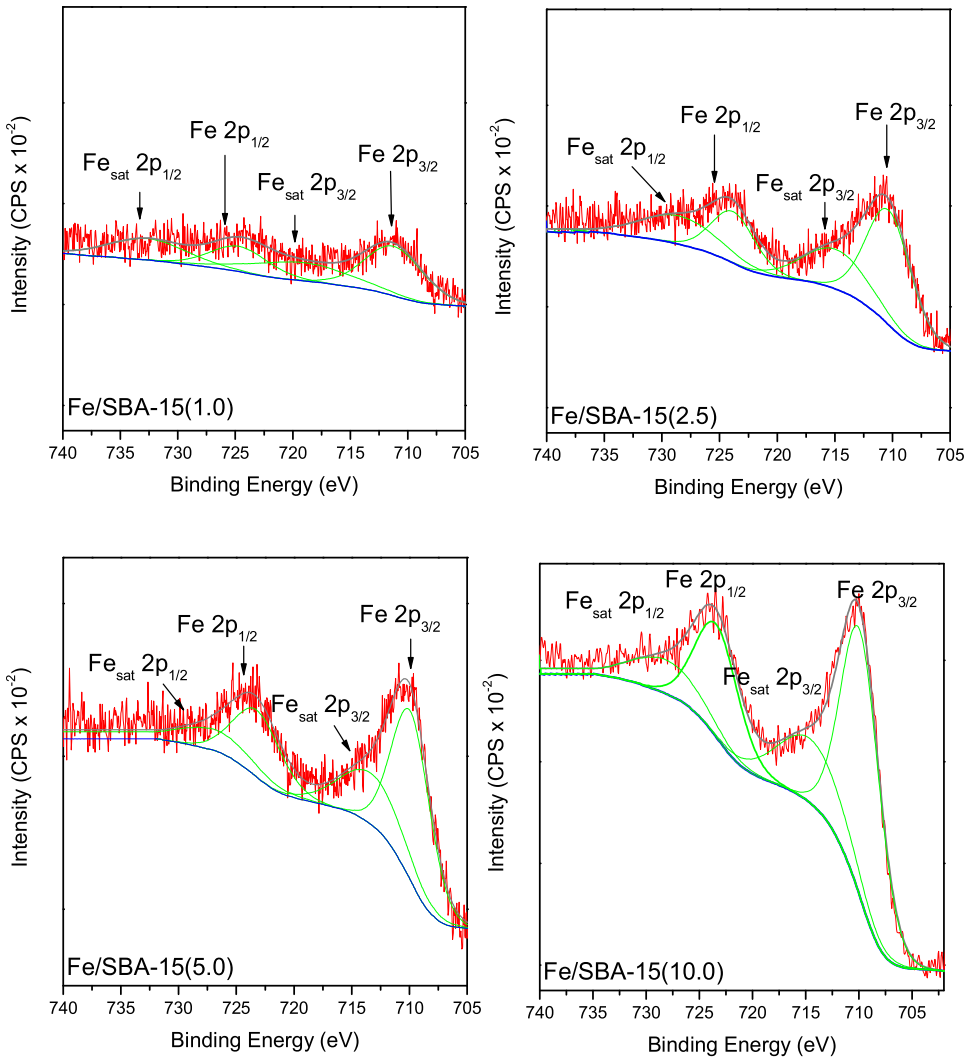

Fig. 11. Fe 2p core level photoelectron profile of Fe/SBA-15(x)350$_{ETOH}$.

from 1.0 to 2.5 wt.%. Instead a mineralization decrease of 10% was observed for the higher loaded samples. These results evidence the major photo-catalytic efficiency of iron species when they are finely dispersed on the surface, present as isolated Fe^{3+} ions, which are proposed as the active sites for the reaction. Meanwhile, when the metal content is increased, the growth of oxide species (as nanoclusters or nanoparticles) could be partially blocking the active sites decreasing their accessibility and catalytic efficiency. In this sense, the bulk oxide Fe_2O_3 hematite was tested as a benchmark catalyst maintaining constant all the other reaction conditions. This test showed a marked decrease in the AO7 degradation (X_{AO7} = 65%) and practically no H_2O_2 conversion (X_{H2O} = 5%) neither mineralization (~0%) were observed. Then, the importance of the isolated Fe^{3+} ions on the surface of a mesoporous silicate of high specific area was verified.

For its part, in order to corroborate the influence of the light irradiation on the catalytic performance of the most active solid, the experiment of AO7 degradation in the dark, but maintaining constant all of the other variables was performed. It was observed that under these conditions the Fe/SBA-15(2.5)350$_{ETOH}$ solid was active for the Fenton process. In this case a high AO7 degradation (X_{AO7} = 90%) and a high H_2O_2 conversion (X_{H2O} = 75%) were observed, but with a marked decrease in the mineralization degree (~65%). It is important to note, that, even if the final AO7 degradation was high, the reaction in dark was notably slower than that assisted with UV_A-Vis light (see Fig. 14 dot-line). Then, taking the mentioned results in mind, Fig. 15 shows the radical species formation pathways proposed for the process in the dark and assisted with UV_A-Vis light. Thus, even if no radiation is present, the finely dispersed Fe^{3+} linked on the SBA-15 surface could react with

Table 4
XPS binding energy (BE) values and surface atomic iron concentrations for Fe/SBA-15(x)350ETOH samples.

Samples	Fe 2p$_{3/2}$ (eV)	Satellite Fe 2p$_{3/2}$ (eV)	Fe 2p$_{1/2}$ (eV)	Satellite Fe 2p$_{1/2}$ (eV)	at.% Fe (XPS)	Surface Fe/Si (XPS)	Bulk Fe/Si (AA)
Fe/SBA-15(1.0)350$_{ETOH}$	711.19	719.14	724.69	732.64	0.28	0.009	0.008
Fe/SBA-15(2.5)350$_{ETOH}$	710.31	714.90	723.81	728.50	0.36	0.011	0.022
Fe/SBA-15(5.0)350$_{ETOH}$	709.87	713.28	723.18	726.88	0.44	0.014	0.065
Fe/SBA-15(10.0)350$_{ETOH}$	709.86	714.54	723.36	728.14	0.74	0.022	0.117

[a]Determined by AA.

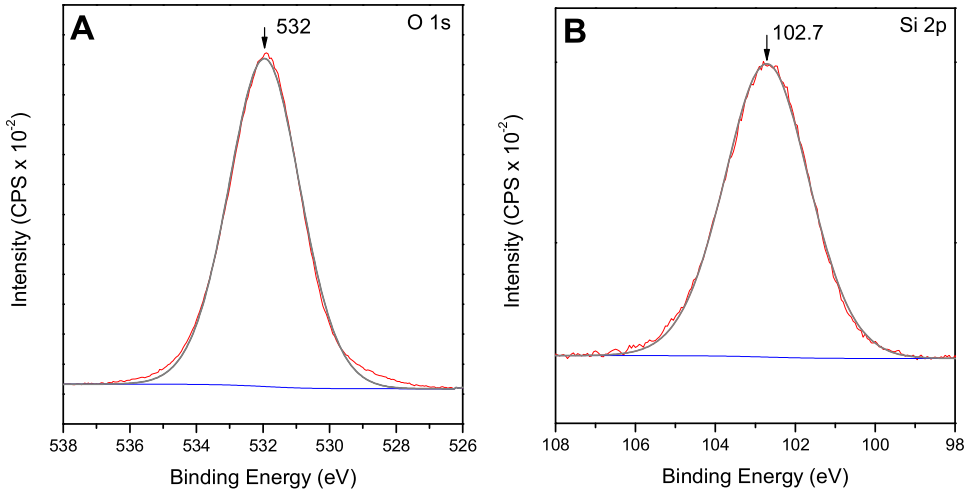

Fig. 12. XPS spectra of (A) Si 2p and (B) O 1s for a representative Fe/SBA-15(x)350$_{ETOH}$ sample.

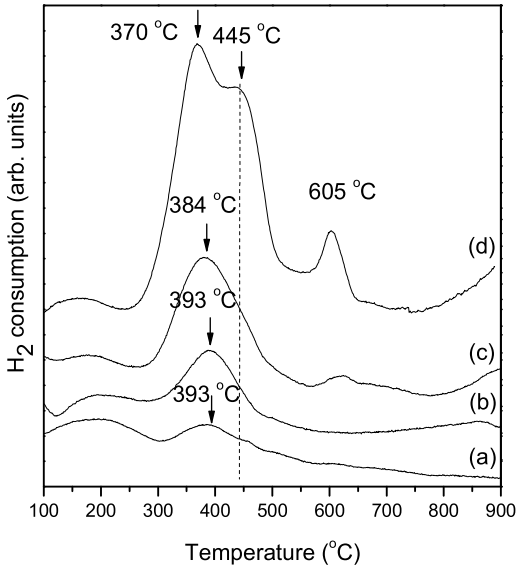

Fig. 13. TPR profiles of Fe/SBA-15(x)350$_{ETOH}$ samples.

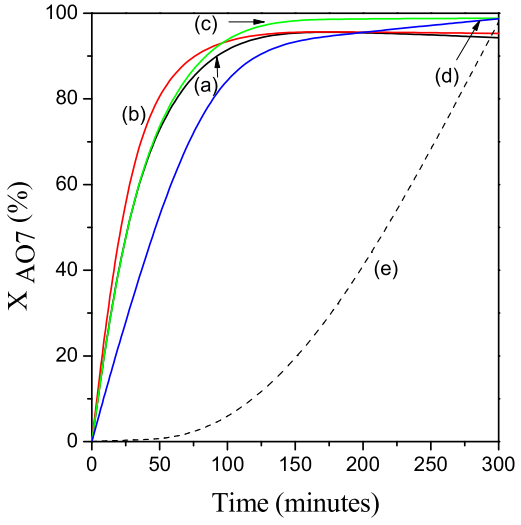

Fig. 14. Percentage of AO7 degradation versus time under UV$_A$-Vis irradiation (pH = 3.5, catalyst concentration = 1 g/L) for the solids: a) Fe/SBA-15(1.0)350$_{ETOH}$, b) Fe/SBA-15(2.5)350 $_{ETOH}$, c) Fe/SBA-15(5.0)350 $_{ETOH}$, d) Fe/SBA-15(10.0)350 $_{ETOH}$ and e) Fe/SBA-15(2.0)350$_{ETOH}$ (without irradiation).

the oxidant molecules H_2O_2, giving rise to the next reactions:

$$Fe^{3+} + H_2O_2 \rightarrow Fe^{2+} + {}^{\cdot}(HO_2) + H^+ \quad (1)$$

$$Fe^{3+} + H_2O_2 \rightarrow Fe-OOH^{2+} + H^+ \quad (2)$$

Then, the Fe^{2+} ions can react with the oxidant and regenerate the Fe^{3+}, according to:

$$Fe^{2+} + H_2O_2 \rightarrow Fe^{3+} + {}^{\cdot}(OH) + (OH)^- \quad (3)$$

In addition, under radiation the photo-Fenton process includes the next reaction:

$$Fe^{3+} + H_2O + h\upsilon \rightarrow Fe^{2+} + {}^{\cdot}(HO) + H^+ \quad (4)$$

Moreover the efficiency of process increases due to the photolysis of hydroxocomplexes of Fe^{3+} which acts as an additional source of radicals:

$$Fe-OOH^{2+} + h\upsilon \rightarrow Fe^{2+} + {}^{\cdot}(HO_2) \quad (5)$$

All the mentioned reactions (Eq. 1–3) involve the formation of free radicals responsible for the organic molecules degradation. Thus, the proposed reactions evidence that high concentration of isolated Fe^{3+} on the surface, promoted by metal nominal loadings of up to 2.5 wt.%, plays a significant role in producing active radical species due to such ions can decompose H_2O_2 molecules to form the already mentioned radical species ${}^{\cdot}OH$ and ${}^{\cdot}(HO_2)$. In addition, these isolated species could also play an important role in adsorbing water molecules to form surface hydroxyl groups, which also promote the ${}^{\cdot}OH$ generation enhancing the degradation process. Therefore, both features would be contributing to the major mineralization observed for the Fe/SBA-15(2.5)350$_{ETOH}$ solid. Moreover, the presence of radiation also enhances the radical species formation, increasing the degradation rate (Fig. 14) and whereas resulting in the higher mineralization degree. In this sense, the degradation rate could be significantly increased using photons which provide additional radicals (Eqs. (4) and (5)).

For its part, it is known that photo-Fenton processes in homogeneous phase can benefit from a wider range of radiation spectrum, as wavelength up to 580 nm were found active for the photoreduction of dissolved ferric iron [39]. According to this, the tests carried out with ferric or ferrous sulfate as homogeneous catalysts led to a complete AO7 degradation and mineralization. Then, considering that the band-gap energy (Eg) is the energy required for the formation of electron-hole (e−/h+) pairs on the semiconductor solid surface, the Eg for the silicates synthesized with different iron loadings were measured using the

Table 5
Catalytic activity of solids synthetized with different iron loadings in the photo-Fenton AO7 degradation.

Sample	X_{AO7} (%)	X_{H2O2} (%)	X_{TOC} (%)	Fe (mg L^{-1})[a]	Eg
$Fe/SBA\text{-}15(1.0)350_{ETOH}$	94.3	93.2	53	0.3	2.42
$Fe/SBA\text{-}15(2.5)350_{ETOH}$	95.3	90.9	81	0.3	2.35
$Fe/SBA\text{-}15(5.0)350_{ETOH}$	98.8	91.8	75	0.3	2.26
$Fe/SBA\text{-}15(10.0)350_{ETOH}$	98.7	94.0	74	0.5	1.94

[a] Iron leaching determined after each catalytic run.

method based on the Kubelka-Munk function fitted as a function of the energy in eV (Table 5) [40]. The obtained low Eg values evidence the ability for the Fe-modified SBA-15 silicates to absorb radiation of low energy. This feature explains the high activity observed for these solids and the high mineralization of AO7 solution reached when UV_A-vis radiation was used. Thus, the presence of the dispersed and linked Fe^{3+} ions on the mesoporous silicate surface provokes an efficient use of radiation and the process could be enhanced in the presence of light. Therefore, the synthetized heterogeneous Fenton catalysts have similar performance to that of homogeneous processes, but with an increased stability which will impact positively decreasing the cost of the treatment process.

On the other hand, although the stability of solids at pH = 3.5 was already tested, it is important to take into account that Fe ions leached even in low concentrations could be active leading to a homogeneous photo-Fenton process contribution. In order to rule out this contribution, the Fe amount leached from solids into reaction medium was determined at the end of each catalytic evaluation. In this sense, for all the samples, not leached Fe^{2+} was measured in the reaction medium. Nonetheless, Fe^{3+} ions can also initiate the homogeneous Fenton process and therefore, the total iron concentration in the medium was also measured. The results from these experiments are presented in Table 5. The low values of leached Fe concentration allow inferring the negligible contribution of the homogeneous process on the mineralization observed for the tested catalysts. It is interesting to note that using the $Fe/SBA\text{-}15(1.0)350_{ETOH}$ a mineralization of 53% was reached and the leached Fe concentration was 0.3 mg L^{-1}. Instead, using the $Fe/SBA\text{-}15(2.5)350_{ETOH}$ a mineralization of 81% was observed with the same

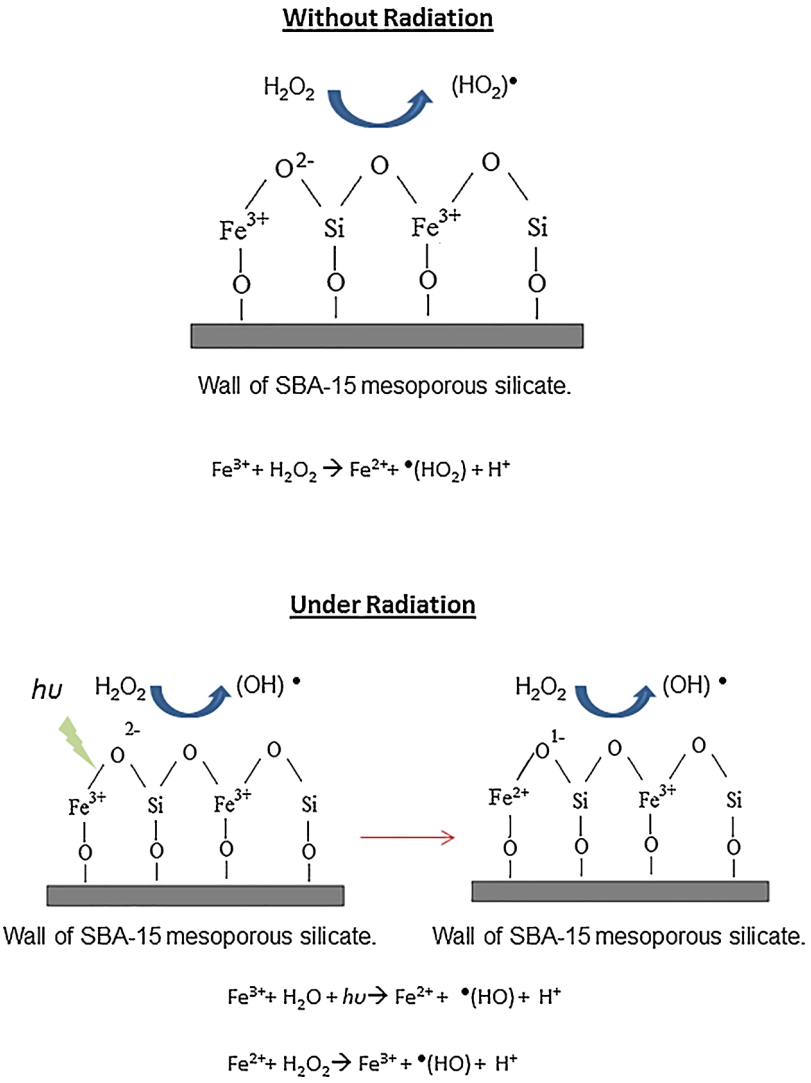

Fig. 15. Radical species generation pathway over the Fe-modified mesoporous silicate surface for the Fenton process without radiation, and under radiation.

concentration of leached Fe. Anyway, in order to verify the importance of the homogeneous reaction on the final degradation results obtained using the Fe/SBA-15(x)350$_{ETOH}$ catalysts, a reaction was performed employing an aqueous solution of Fe^{3+} (0.3 mg L^{-1}) as homogeneous catalyst. This test resulted in a 27% of AO7 degradation and no mineralization. Taking into account that using Fe/SBA-15(2.5)350$_{ETOH}$ the almost complete AO7 and H_2O_2 conversion and very high mineralization degree could be reached, it is possible to claim that he homogeneous catalytic reaction is not significant. Then, these results give account for the major contribution of the heterogeneous process. Nonetheless, in order to further evaluate the stability of this catalyst, it was recovered from the reaction medium after its use, calcined at 350 °C and again evaluated. The same mineralization degree was obtained when Fe/SBA-15(2.5)350$_{ETOH}$ was used after a second catalytic run confirming its stability and reuse capacity. Therefore, it is possible to affirm that the solids are actually acting as heterogeneous photocatalysts and can be reused for a t least two cycles. A nominal Fe loading of 2.5 wt.% arises as optimal in order to reach a high proportion of active Fe^{3+} sites finely dispersed and accessible on the surface.

4. Conclusions

Mesoporous molecular sieves with SBA-15 structure were modified with iron by the wet impregnation method employing different solvents, calcination temperatures and metal loadings. All solids presented good structural ordering and high areas, P_v and P_D. It could be inferred the presence of three different Fe species formed on the structure: isolated Fe^{3+} cations, iron oxides such as (FeO)n nanoclusters and bigger oxides as nanoparticles. The use of ethanol as solvent favored the presence of iron species finely dispersed and highly stabilized mainly on the internal walls of the mesopores. In fact, such solids resulted highly stable to the metal leaching in presence of H_2O_2 aqueous solution at pH = 3.5 for long times of contact. This behavior was attributed to the lower polarity of ethanol that allows the better dispersion of the metal precursor during the impregnation, giving rise to the formation of the isolated iron species strongly anchored on the surface. The calcination temperature did not influence notably on the iron speciation. The lower iron loadings also led to higher relative percentage of isolated Fe^{3+} ions strongly linked to the surface and of hardly reducibility. Meanwhile, a higher proportion of bigger iron oxides was observed for the higher loadings.

The catalyst prepared with a nominal Fe loading of 2.5 wt.%, using ethanol as impregnation solvent and calcination at 350 °C, allowed to reach the highest mineralization (81%) of AO7 during the photo-Fenton process under UV_A-vis at pH = 3.5. This fact gives account of the efficiency of iron species when they are finely dispersed and accessible on the surface, mainly as isolated Fe^{3+} ions. The heterogeneity of the catalytic process could be confirmed. The catalyst was highly stable and could be reused remaining its high performance.

Acknowledgements

VRE, EGV, CHI, SGC and GAE are research members of CONICET, Argentina. Authors are grateful to UTN and CONICET for the financial support. SAXS experiments at INIFTA were performed thanks to project “Nanopymes” (EuropeAid/132184/D/SUP/AR-Contract-896). Thanks are given to ANPCyT for the purchase of the SPECS multitechnique analysis instrument (PME8-2003).

References

[1] E. Bizani, K. Fytianos, I. Poulios, V. Tsiridis, J. Hazard. Mater. 136 (2006) 85–94.
[2] M. Catanho, G. Malpass, A. Motheo, Appl. Catal. B 62 (2006) 193–200.
[3] I. Konstantinou, T. Albanis, Appl. Catal. B 49 (2004) 1–14.
[4] A. Dhakshinamoorthy, S. Navalon, M. Alvaro, H. Garcia, Chem. Sus. Chem. 5 (2012) 46–64.
[5] J. Yang, K. Hidajat, S. Kawi, J. Mater. Chem. 19 (2009) 292–298.
[6] S. Zheng, L. Gao, Q.H. Zhang, W. Zhang, J.K. Guo, J. Mater. Chem. 11 (2001) 578–583.
[7] A. Bokare, W. Choi, J. Hazard. Mater. 275 (2014) 121–135.
[8] S. Rahim Pouram, A. Abdul Raman, W. Wan Daud, J. Cleaner Prod. 64 (2014) 24–35.
[9] H. Zhang, Y. Dong, W. Fang, Y. Lian, Chin. J. Catal 34 (2013) 330–335.
[10] J. Zhang, Z. Xin, X. Meng, Fuel 116 (2014) 25–33.
[11] X. Zhang, D. Wang, J. Peng, C. Lu, L. Xu, J. Fuel Chem. Technol. 43 (2015) 243–250.
[12] F. Guo, S. Guo, Z. Qiu, J. Braz. Chem. Soc. 25 (2014) 750–758.
[13] Y. Shu, L. Murillo, J. Bosco, Appl. Catal. A Gen. 339 (2008) 169–179.
[14] J. Sietsma, J. Meeldijk, M. Versluijs-Helder, Chem. Mater. 20 (2008) 2921–2931.
[15] M. Tao, X. Meng, Y. Lv, Z. Bian, Z. Xin, Fuel 165 (2016) 289–297.
[16] J. Pignatello, E. Oliveros, A. Mackay, Environ. Sci. Technol. 35 (2006) 1–84.
[17] E. Neyens, J. Baeyens, J. Hazardous Mater. 98 (2003) 33–50.
[18] A. Greenberg, L. Clesceri, A. Eaton, Standard methods for the examination of water and wastewater, 18th ed., American public health association, American Water Works Association, Water Pollution Control Federation; Joint Editorial Board, Washington, DC, 1992.
[19] A. Allen, J.A. Hochanadel, J. Ghormley, T. Davis, J. Phys. Chem. 56 (1952) 575–586.
[20] S. Förster, A. Timmann, M. Konrad, C. Schellbach, A. Meyer, S. Funari, P. Mulvaney, R. Knott, J. Phys. Chem. B 109 (2005) 1347–1360.
[21] J. Feng, X. Hu, P. Yue, Environ. Sci. Technol. 38 (2004) 5773–5778.
[22] S. Hosseini, R. Ahmadi, A. Ghavi, A. Kashi, Powder Technol. 278 (2015) 316–322.
[23] D. Barrera, J. Villarroel-Rocha, L. Marenco, M. Oliva, K. Sapag, Adsorp. Sci. Technol. 29 (2011) 975–988.
[24] H. Zhang, J. Sun, D. Ma, X. Bao, A. Klein-Hoffmann, G. Weinberg, D. Su, R. Scho, J. Am. Chem. Soc. 126 (2004) 7440–7441.
[25] V. Elías, M. Oliva, S. Urreta, K. Sapag, A. Mudarra, S. Casuscelli, G. Eimer, Appl. Catal. A Gen. 381 (2010) 92–100.
[26] N. Cuello, V. Elías, C. Rodriguez Torres, M. Crivello, M. Oliva, G. Eimer, Microporous Mesoporous Mater. 203 (2015) 106–115.
[27] H. Zhou, K. Li, B. Zhao, W. Deng, Y. Su, F. Zhong, Chem. Eng. J. 326 (2017) 737–744.
[28] N. Fairley. CasaXPS Version 2.3.15 copyright 1999–2009.
[29] P. Mills, J. Sullivan, J. Phys. D 16 (1983) 723–732.
[30] D. Hawn, B. DeKoven, Surf. Interface Anal. 10 (1987) 63–74.
[31] M. Muhler, R. Schlögl, G. Ertl, J. Catal. 138 (1992) 413–444.
[32] A. Grosnover, B. Kobe, M. Biesinger, N. McIntyre, Surf. Interface Anal. 136 (2004) 1564–1574.
[33] S. Shylesh, P. Samuel, A. Sing, Appl. Catal. A Gen. 318 (2007) 128–136.
[34] V. Elías, E. Vaschetto, K. Sapag, M. Oliva, S. Casuscelli, G. Eimer, Catal. Today 172-1 (2011) 58–65.
[35] M. Mokhonoana, N. Coville, Materials 2 (2009) 2337–2359.
[36] K. Lázár, G. Páz-Borbély, A. Szegedi, H. Beyer, Stud. Surf. Sci. Catal. 142 (2002) 1347–1354.
[37] Q. Ma, K. Klier, H. Cheng, J. Mitchell, K. Hayes, J. Phys. Chem. B 104 (2000) 10618–10626.
[38] P. Maniar, A. Navrostsky, J. Non-Cryst. Solids 120 (1990) 20–25.
[39] R. Bauer, G. Waldner, H. Fallmann, S. Hager, M. Klare, T. Krutzler, S. Malato, P. Maleztky. Catal. Today 53 (1999) 131–144.
[40] R. López, R. Gómez, J. Sol-Gel Technol. 61 (2012) 1–7.